12

Nanoporous Alumina Templates: Anodisation and Mechanical Characterisation

Anura P. Samantilleke*, J.O. Carneiro*, P. Alpuim,
V. Teixeira and Tran Thi Thu Thuy

ABSTRACT

Due to applications in electronics, optoelectronics, energy storage, photocatalysis, photonics and biosensors/biomaterials, interest in one-dimensional nanostructures has grown significantly during the last decade. The use of nanoporous templates as matrices for fabrication of nanostructures is now commonplace in microelectronics technology. Studies on semiconductors and dielectrics have introduced nanoporous anodised aluminium oxide as a very promising template material for the deposition of nanostructures. It is formed of an array of closely packed hexagonal oxide cells, in the centre of each of which there is a vertical hollow channel, fabricated by simple electrochemical anodisation. Anodisation, an economically viable electrochemical process, has been extensively investigated over a number of years to obtain protective and decorative films on an Al surface. The advantages in using these templates are controllability of the pore size, ratio aspect and use of low cost and simple equipment. Nanoindentation, a method that makes use of very low loads in the millinewton range has been widely used for measuring mechanical properties such as the hardness and Young's modulus of test samples. In the first part of this chapter, the anodisation of alumina templates, as well as the electrochemical process parameters and mechanisms are discussed by means of structural and morphological characterisation. The second part is dedicated to the study of mechanical properties of nanotemplates using nanoindentation.

[1] Centro de Física, Universidade do Minho, Azurém, 4800-058 Guimarães, Portugal
**Corresponding author*: E-mail: anura@fisica.uminho.pt

***Key words*:** Nanopores, Electrochemical, Alumina, AAO, Nanoindentation, Hardness, Young´s modulus

1. INTRODUCTION

1.1. Synopsis

Nanostructured materials are of practical and scientific interest both for understanding the fundamental electronic, magnetic, optical, thermodynamic, and mechanical properties of materials with nanometer sizes and for producing structures with radically new physical properties, resulting in significant increases in the functional characteristics of electronic and optical devices. In recognition of applications in electronics, optoelectronics, energy storage, photocatalysis, photonics and biosensors during the last decade, interest in one-dimensional nanomaterials such as nanotubes, nanorods and nanowires has grown significantly in both research and industrial settings[1]. The use of nanoporous materials as matrices for deposition or technological masks for etching and doping is now commonplace in microelectronics technology. Studies on porous semiconductors and dielectrics have introduced a very promising material for the deposition of nanostructures, porous anodised aluminium oxide (AAO). It is formed of an array of closely packed hexagonal oxide cells, in the centre of each of which there is a vertical hollow channel, fabricated by simple anodisation, an economically viable technique.

Anodisation, an electrochemical process used to increase the thickness of the naturally occurring oxide layer on Al not only in industry, but also in science, has been extensively investigated to obtain protective and decorative films on an Al surface. Nanoporous alumina materials and structures are usually prepared by metal anodisation, using electrolytes in which the oxide is slightly soluble, a process that has been investigated in detail for over 60 years.

The structure of AAO, which has been found to be stable at high temperature and in organic solvents, exhibits uniform pore density, and the pores are parallel and perpendicular to the surface, having an ideal cylindrical shape (Fig. 1(a)). A scanning electron microscopy (SEM) image of a nanoporous AAO surface is shown in Fig. 1(b).

Every pore is embedded in a hexagonal cell structure. The cell walls are made of Al_2O_3, which run parallel along the entire length of the template and terminate at the bottom of the pores in hemispherical shells termed as the barrier layer, which has tremendous significance in the mechanism of formation, structure and size of the AAO formed. In nanoporous AAO structures, the pore diameter and periodicity as well as the narrow distribution of pore size are easily controllable. Besides porosity, it shows an

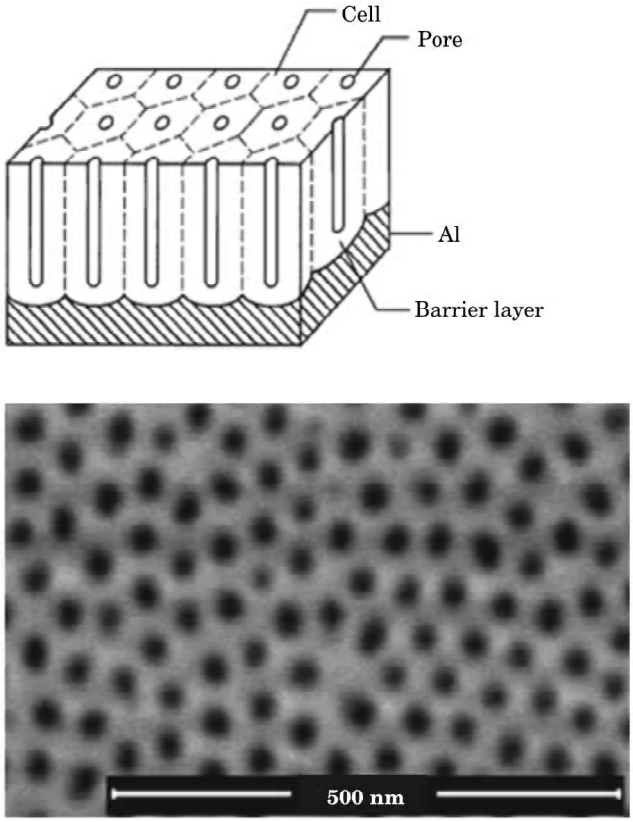

Fig. 1: (a) A schematic drawing of porous alumina. The geometry of porous alumina may be schematically represented as a honeycomb structure of fine channels characterized by a closed-packed array of columnar hexagonal cells, each containing a cylindrical pore at the centre[2]. (b) A bird's eye view of a nanoporous AAO surface.

excellent thermal shock resistance, good thermal insulation and good chemical resistance[3]. The formation of the AAO membrane is dependent on the electrolyte composition (type and concentration), anodisation time, applied voltage, temperature and pre-treatment methods. The pore size is also controlled by the pore-widening treatment, dipping the porous alumina in an acidic electrolyte after the anodisation. Often the AAO fabrication process comprises more than one separate anodisation step. However, the degree of the ordering of the pore configuration at the surface of the anodic porous alumina is low after one step, because the pores develop randomly at the initial stage of the anodisation. In order to improve the ordering of the surface side of the anodic porous alumina, two-step anodisation is usually preferred.

AAO templates are suitable for many technical applications, such as lithography-free nanopatterning, the fabrication of highly ordered metallic

nanowire arrays, the growth of carbon nanotubes or the realization of nanocapacitor arrays. Also these templates have been frequently used for synthesis of nanomaterials because they not only have the pores in high ordering but also are reproducible and economical. Besides, it is not limited by the choice of materials[4]. AAO can further be used as a template for fabrication of nanocomposite structures or biomaterials[5]. The advantages when using these templates are controllability of the pore size, ratio aspect and use of low cost, simple equipment comparing with electron beam lithography, ion beam lithography or X-ray lithography. AAO templates can have important medical applications in drug delivery and fluid separation. For example, in hemodialysis, a pore size that is capable of clearing small (urea, creatinine) and middle (vancomycin, inulin) molecular weight solutes while maintaining large molecular weight molecules (albumin) is the most desirable[6]. The fabrication of ordered arrays of functional biomolecules such as proteins, DNA, and enzymes is important because of its potential for application in several kinds of biomolecular nanodevices. The use of highly ordered anodic porous alumina results in the efficient formation of ordered arrays of biological molecules[7]. AAO can also be used to fabricate capacitive humidity sensors because the structure has nanosized pores, giving it a large surface area for absorbing water vapour. A thick porous layer or large pore diameter increases sensitivity because of increase in contact surface area[8]. Chemically functionalised AAO membranes can be utilized for catalytic or optical purposes. Furthermore, the porous AAO membrane itself is employed for filtration, gas separation or as photonic crystals[9].

1.2. Background

Templates consisting of nanopores with uniform diameter and length are regularly used to fabricate uniform nanostructures. Fabricating such templates with uniform pore diameters holds the key to controlling the size and the shape of nanostructures[10]. Electrochemical methods have been used to fill nanopores in the template with conducting, semiconducting or bio-molecular materials, in order to fabricate nanostructures and integrate them in circuit components[11]. Porous anodic aluminium oxides (AAO) have been attracting considerable attention in both scientific and commercial fields as an indispensable part of nanotechnology[12]. In 1970, O'Sullivan and Wood presented a model to describe self-regulating pore growth[13]. During the anodisation process within an acidic medium, the Al surface is oxidized where the oxide layer consists of a self organized nanoporous structure. Interest in AAO nanostructures and their fabrication using the two-step anodisation process has recently been reinvigorated, as described by Masuda and Fukuda[2]. A two-step anodisation process is deemed essential in order to regulate the nanoporous structure, since irregular nanopores are formed on the Al substrate after the first anodisation.

However Kirchner and co-workers fabricated AAO membranes by one-step anodisation process[14]. In their work, Al electrodes (25 mm × 10 mm) were degreased in acetone and cured for 2 h at 80ºC. The specimens were anodised in 0.3M H_2SO_4 electrolyte for about 12 h at a constant potential of 25.0V with a platinum cathode, at 7ºC using a stirred double jacketed vessel connected to a thermostat. After anodisation, the remaining aluminium metal was dissolved in a saturated iodine–methanol solution at 50ºC. The transparent porous anodic alumina membranes were rinsed in methanol to clean off excess iodine. Subsequently the pores on the metal contact side of the film were opened by etching in 5% H_3PO_4 for 60 min at 30ºC. A three-step anodisation has also been used as a method to fabricate self-organized nanopores in oxalic and sulphuric acid. Often, the time intervals for three steps are different. For example, Feiyue Li *et al.* used 5–10 mins, 0.5–12 hours and 3 min for the three respective steps in their anodisation of Al[15]. It was found that the order of self-assembled nanopore structures is comparable between the three-step anodisation, and the two-step anodisation processes. Brändli *et al.* used 0.3 wt% oxalic acid electrolyte for anodising Al and a wet chemical etching solution, comprising 1:1 chromic acid (0.4%) and phosphoric acid (0.6%), for selective aluminium oxide stripping[16]. The electrode was immersed in this solution for 6 min at 60°C for each etching step. They showed that increasing the number of anodisation-etching cycles leads to an increase in the uniformity of the pore size and the pore diameter. However, two-step anodisation generates an ordered pore array throughout the entire oxide layer. Well-ordered nanopore arrays are obtained by etching out the oxide layer with irregularly arranged nanopores towards the film surface. Using this two-step method, Masuda and Fukuda obtained a well ordered and hexagonal nanopore array (Fig. 1).

Formation of the pores in anodic metal oxides is described by the plasticity model where it is believed to be a consequence of flow of film material in the barrier layer region beneath the porous layer. The material flows from the region of pore bases towards the cell wall regions due to growth stresses and field-assisted plasticity of the film material[17-19]. However, the formation mechanism of the pores is more complicated than previously thought[20]. Although the formation mechanism, pore ordering, inter-pore distance and pore size control have been extensively studied, there is much work still to be done in order to understand the electrochemistry and the anodisation process. The applied potential in anodisation varies with the type of the electrolyte used. The effect of a variety of acids has been investigated resulting in varying degrees of success as determined by the pore ordering of the arrays obtained[21]. Sulphuric acid proves to be the most commonly used acid among the more effective electrolytes. When characterizing nanopore arrays, nanoindentation is a technique providing invaluable information such as the hardness and the elastic modulus of the nanostructure investigated[22]. Xia *et al.* studied the

effect of heat treatment on AAO showing that heat treatment up to a maximum of 600ºC leaves the elastic modulus unaffected[23].

2. ELECTROCHEMICAL PROCESS OF FABRICATING AAO

2.1. Two-Step Anodisation Method

As proposed by Masuda and Fukuda, AAO templates are produced by two-step anodisation on pre-cleaned Al substrates. The effect of pre-treatment is discussed later in detail. The pre-cleaned Al electrodes will undergo the first step of the two step anodisation. Here, by applying an appropriate potential against a Pb cathode in an acidic electrolyte, the surface of the etched Al surface is roughened to a shell-like morphology and ordered into a hexagonal porous array. Although several acids can be used and are essential for fabricating different pore sizes, sulphuric acid is the most commonly used electrolyte. With sulphuric acid (H_2SO_4), templates with maximum pore diameter about 40 nm can be obtained. The process usually is carried out in 0.3M H_2SO_4 at 5ºC and by applying 40V anodisation potential. The divots formed in pores on the AAO structure is then etched out in a chromophosphoric solution (H_3PO_4 8% vol + Cr_2O_3 4% wt). The base of the divots will initiate new pore formation and thus the Al substrate is ready for a second anodisation, the templating process that results in the highly ordered nanoporous structure. This step is similar in terms of anodisation conditions such as the applied potential, temperature and concentration of acid but different in duration of the anodisation. The duration of the first anodisation is generally about 1hour whereas that of the second anodisation varies from 2 to 7 hours depending on the desired pore size.

2.2. Current Density and Pore Formation

A typical current density plot during the anodisation of Al foils (99% purity) in 0.3 M H_2SO_4 acid is shown in Fig. 2, which consists of three noticeable current density regions for the formation of porous alumina.

At the initial stage (region A), a barrier layer is first formed on the aluminium surface when the potential is applied[24]. With the growth of the oxide barrier layer through the relatively fast reaction at the very early stages of the process, the resistance of the electrode increases resulting in a sharp decrease in current density, as shown in the region 'a' of the inset. With this process, transport of Al^{3+} ions and their ejection to electrolyte results in a slow increase in the current density (region 'b'). However, steady current density is observed as shown in region 'd', when equilibrium is achieved between the AAO formation and the Al^{3+} ion ejection ('c' and 'd'). Singh *et al*. attributed the pore initiation and self organization of the porous structures at the initial stage to the considerable elastic stress in the oxide

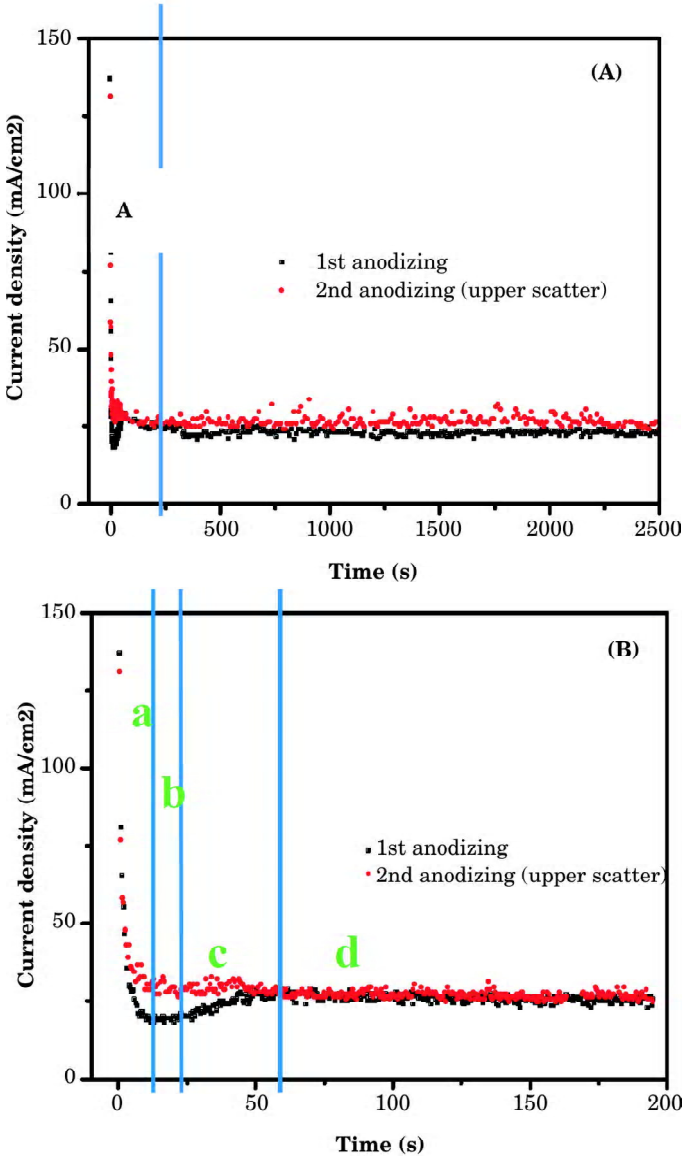

Fig. 2: (a) Current density j(t) monitored during anodisation in 0.3M sulphuric acid, Uap = 20V, T= 5°C, for a first anodisation (black line) and j(t) for the second anodisation (red line) following a two-step anodisation process.(b) Region A of (a)

layer[25]. Although the phenomenological description that the mechanical stress inflicted by the volume expansion on the structure due to the difference in ionic densities of Al^{3+} and Al in anodic alumina, a consequence of the difference in mass densities was possibly accountable for the self-

organized formation of hexagonal pore arrays (Fig. 1)[26]. Hence the pore formation and the porous film growth is better described using the "Plastic ionic flow model", where the pore formation in the anodized oxide is explained in terms of mass migration of metal ions within the oxide from underneath the pores to pore wall. As described in the literature, barrier-type anodic alumina films grow by migration of Al^{3+} ions outward and $O^{2"}$ ions inward[27]. As Thompson described, about 40% of the film thickness forms at the AAO film/electrolyte interface as a result of the migration of Al^{3+} ions for growth at 100% efficiency. The remainder of the film thickness is formed at the metal/film interface by migration of $O^{2"}$ ions[28]. The formation of the porous film takes place when there is no film material being added at the Al_2O_3/electrolyte interface. According to Thompson *et al*, this corresponds to an efficiency of about 60% for conditions close to those presently used for anodisation. Whilst increased stresses from electrostriction assist stabilization of the pores, the absence of growth of new oxide at the film surface prevents pore-filling.

Although in general the current densities of the first and the second anodisation demonstrate similar overall behaviour over time, certain differences have also been observed. The lowest apparent current density is generally higher for the second anodisation step than for the first and the time taken to reach the constant current density during the second anodisation is shorter than that in the first step. This irregularity can be attributed to the fact that in the first anodisation step the porous structure is not yet formed, while in the second anodisation, the patterning of the pores has already taken place, after removing the aluminium oxide layer by etching in chromophosphoric acid solution (H_3PO_4 and H_2CrO_4).

2.3. Chemical Reactions

The reactions during anodisation under steady state conditions take place across the barrier layer. Reactions related to formation of pores occur at both the Al/Al_2O_3 interface and the Al_2O_3/electrolyte interface through ion migration across the barrier layer. As has been reported previously, the dissociation of water supplies anions to the oxide layer, but also plays an important role in governing the porosity of the porous AAO films[29]. While the anions, O2- or OH- ions, drift towards the Al/Al_2O_3 interface, Al^{3+} ions drift towards the Al_2O_3/electrolyte interface. Eventually Al^{3+} ions are ejected into the electrolyte, which results in the dissolution of Al_2O_3 (Equation 1a).

$$Al_2O_3 + 6H^+ \rightarrow 2Al^{3+}_{(aq)} + 3H_2O \quad (1a)$$

In the meantime, reaction between Al and the anion produced by water continues to produce Al_2O_3 (Equation 1b).

$$2Al + 3H_2O \rightarrow Al_2O_3 + 6H^+ + 6e^- \quad (1b)$$

The dynamic equilibrium between the two reactions at steady state facilitates self assembly of the porous AAO structure.

2.4. Mechanism of Self-Assembly of Nanopores

According to the phenomenological model, self-assembly and ordering is a result of the mechanical stress associated with the volume expansion during the oxide formation on Al since simultaneous growth of pores restricts Al_2O_3 to growing perpendicular to the Al surface. The porous structure self-orders under steady state, when the mechanical stress generated between the pore walls is equilibrated.

Among the other models proposed to describe the mechanism of self-assembly, the simple electrostatic model of the field-assisted dissolution of the barrier layer or the plasticity model has been widely accepted[30]. According to the model, the electric field at the Al_2O_3/electrolyte interface responds to any change in pore sizes during anodisation. The electric field increases whenever the pore diameter decreases from its equilibrium value, increasing the field assisted dissolution rate, which eventually will cause the pore diameter to increase. The self-assembly of the pore structure is governed by electric field changes to the pore surface morphology, which counteract any physical changes. The film material in the barrier layer region beneath the porous layer will flow from the region of pore bases towards the cell wall regions due to growth stresses and field-assisted plasticity of the film material.

2.5. The Effect of the Electrolyte and Supporting Evidence

The two-step anodisation process is commonly used to fabricate AAO with different types of electrolyte such as sulphuric acid, oxalic acid and phosphoric acid. For each electrolyte, one has to choose applied voltage, temperature of electrolyte, time of anodisation and concentration of acid to get optimized pores. This restriction in choice of conditions for anodisation is due to the conductivity and pH value of the electrolyte. For example, if aluminium is anodized in sulphuric acid at a relatively high potential (note that sulphuric acid has a very high conductivity), the oxide layer breaks down easily. In addition, the pH-value of the electrolyte determines the size of the pores. The lower the pH value, the lower the potential threshold for field-enhanced dissolution at the pore tip, which leads to a smaller pore sizes. Therefore, large pore diameters are formed by using the oxalic or phosphoric acid and small pore diameters are obtained by using sulphuric acid.

For example, Xin Wang *et al.* worked with 0.3M oxalic acid, and the applied voltage was 30-50 V at room temperature[31]. The results show distinctly an ordered honeycomb structure with uniform pore-diameter and

inter pore-spacing fabricated with this method. The pore diameter was 20 nm and pore spacing was 80 nm for AAO when 40 V was applied, while the application of 50 V caused pore-size to be 35 nm in diameter and 110 nm in spacing. A. Belwalkar *et al.* used 2.7 wt% oxalic acid and anodised Al under different voltages at 0ºC[32]. The pore diameter and the interpore distance were 18.6 ± 2.9 and 65.1 ± 6.5 respectively under an applied potential of 30V whereas they were 33.6 ± 7.6 and 80.5 ± 3.2, respectively under 40V applied potential. Although pores with smaller diameter (~18 nm) can be made with oxalic acid, significantly large pore sizes can also be made. In contrast, Fig. 3 shows (a) an SEM image and (b) an atomic force microscopy (AFM) image of an AAO template surface after the two anodisation steps in 0.3M sulphuric acid. Templates with nanopores of a uniform size exhibit an almost perfect 2-D array with a hexagonal pattern. The average diameter and interpore distance are 26 ± 1 and 42 ± 2 nm, respectively, which are the highest dimensions that can be achieved when using sulphuric acid. Here, the pore density is about 2.7×10^{10} pores/cm^2.

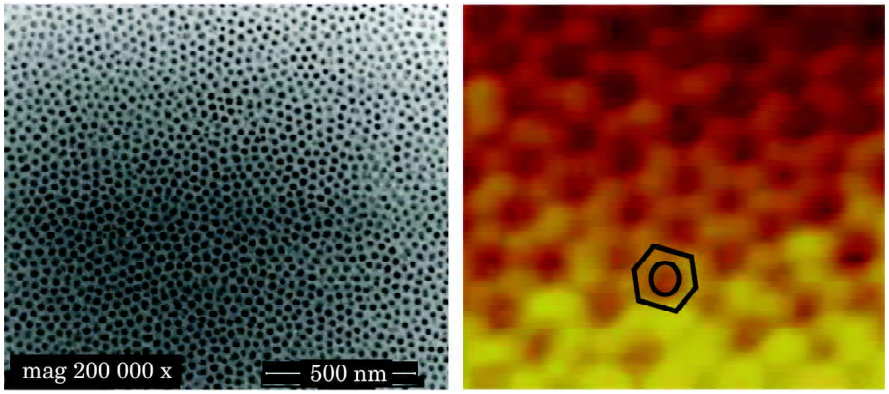

Fig. 3: SEM images of the surface of AAO templates (a) after the second anodization, and (b) after pore widening

C.T. Sousa *et al.* investigated nanoporous self-organized AAO templates, where both the anodisation steps were carried out in 0.3M H_2SO_4 at voltages 15V, 20V and 25V, for 2h, at temperature 12 ± 2ºC[33]. The results of this research are an applied potential of 25V giving the best conditions for the appearance of organized patterns. There is a confinement of pore order to the aluminium grains. The anodisation at 25V gave the largest interpore distance in the aluminium (~30 nm).

Jaime Martín *et al*. used a phosphoric acid/methanol/water mixture (1:10:89, weight proportions) electrolyte, and anodised under a constant potential of 195V and at -4ºC (methanol was added to the electrochemical

bath in order to avoid the electrolyte from freezing)[34]. To avoid completely the breakdown, the voltage at the beginning was 185V and increased to 195V after 4h. The first anodic layer was then removed by chemical etching in a mixture of phosphoric acid (7 wt.%) and chromic oxide (1.8 wt.%). Finally, the second anodisation was performed in the same conditions as the first, but directly under 195V. The results were pore diameter 137nm and interpore distance 447 nm.

Leszek Zaraska *et al.* also fabricated AAO templates by a two-step process under a constant voltage (110, 160, 170 V) in a 0.3 M H_3PO_4 electrolyte or an alcohol at the temperature of 0 or "5 ± 0.02°C[35]. The duration of each anodisation step was 8 h. The alumina layer formed during the first step of anodisation was removed by chemical etching in a mixture of 6 wt% H_3PO_4 and 1.8 wt.% H_2CrO_4 at 60°C for 2 h. After the oxide removal, the second anodisation was performed under the same conditions as in the first step. The anodisation potential had no effect on the pore circularity for samples made in 0.3 M H_3PO_4 electrolyte while the complex pore structure with sub-pores were formed underneath the film surface. However, the regularity of pore arrangement and uniformity of pore structure increased with the potential, independent of the electrolyte composition. The interpore distance of pore structure of AAO films increased from 342 nm to 478 nm when anodisation potential was increased from 110 V to 160 V. Younghee Na *et al.* however used a different approach, where they used two different electrolytes for the two steps of anodisation, namely 0.2 M phosphoric acid in the first anodisation and 0.2 M oxalic acid in the second anodisation step[36]. The synthesized AAO templates could be successfully used to obtain highly ordered nanometer-sized wires for large area device applications.

Electrolytes such as citric acid, chromic acid and tartaric acid, have also been used with varying success elsewhere[37]. In summary, the relationship between the conditions for fabrication AAO templates in common electrolytes are given in Table 1.

Table 1: Structural features of nanostructure obtained by anodizing in various conditions

Electrolyte	***Voltage (V)***	***Pore diameter (nm)***	***Inter-pore distance (nm)***
Phosphoric acid (H_3PO_4)	100-195	130-250	250-500
Oxalic acid ($H_2C_2O_4$)	30-80	40-100	80-200
Sulphuric acid (H_2SO_4)	15-25	15-25	60-70

2.6. The Effect of Pre-Treatment

The quality of surface of substrates has major influences on the nanostructure by self-organized anodisation. The surface of the alumina

film can be modified thermally or by electrochemical and chemical pre-treatment. The pre-treatment process accelerates the reduction in surface defects. Fratila-Apachitei *et al*. investigated the influence of substrate microstructure on the growth of anodic oxide layer, the results of which showed that the uniformity of the oxide growth increased with the increasing purity of aluminium[38].

Among various solvents used for degreasing, acetone and ethanol are commonly employed. Other often used chemicals are, such as dichloromethane[39], trichloroethylene[40], benzene and methanol. The immersion of samples in 5% NaOH at 60ºC for 30s or 1 min and subsequent neutralization in a 1:1 HNO_3 + H_2O solution for several seconds was also proposed for Al degreasing and cleaning[41-43]. A mixed solution of HF + HNO_3 + HCl + H_2O (1:10:20:69) was also used for degreasing and cleaning of the aluminium surface[44]. *D.C. Leitão et al*. studied how different chemical and physical pre-treatments of high purity (99.997%) aluminium foils, influence nano-pore growth and inter-pore organization upon anodisation in 1.2 M H_2SO_4 for 1 hour, at room temperature. After degreasing in ethanol, samples were immersed in 1 M NaOH for native oxide removal, diamond

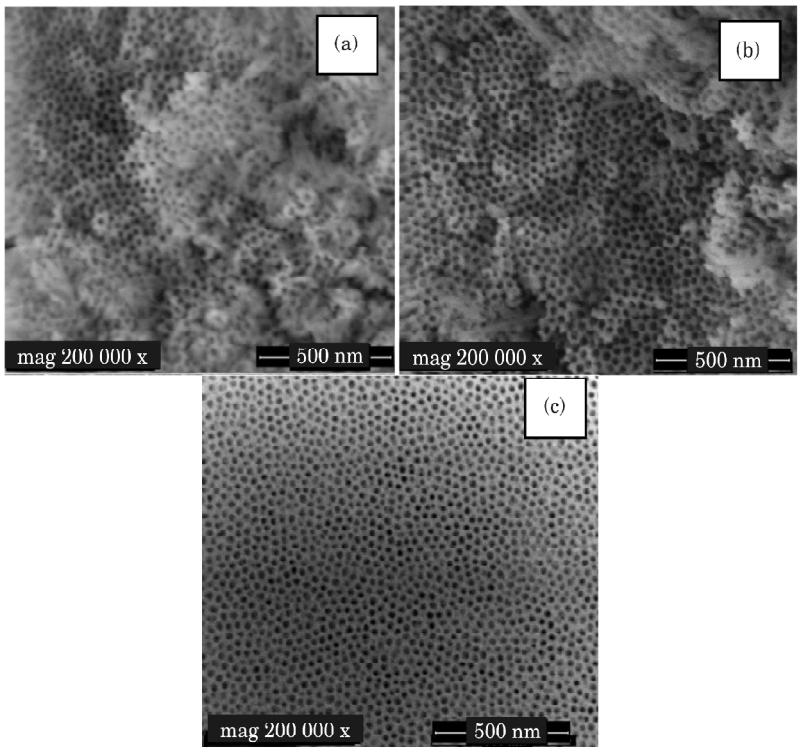

Fig. 4: Samples with different pre-treatments a. In benzine for 1min (Al5); b. in NaOH for 5 min (Al6); c. in benzine for 2min (Al7)

paste polished, electropolished and ion-milled. They obtained that the smoothness of Al-foil surface is crucial in order to get a good quality porous structure. Pre-treatment with NaOH etching gives the best results for good quality and, to a certain extent, organised pore structures[45].

Fig. 3 shows three samples following different pre-treatment processes. In the two samples treated in benzine for 1min and NaOH for 5 min (Al6), the physical parameters of the AAO are similar. However, the morphology of the surface is uneven; the pores can be seen at different levels. In contrast, in the sample etched in benzine for 2 min (Al7), the surface is found to be more uniform.

2.7. Pore Size Analysis

The SEM images in Fig. 4(b-d) show the well-defined, self-ordered, porous alumina obtained. Samples anodized in different concentrations of electrolyte (1 M and 0.3 M), different applied potentials (17 V and 20 V) and at the same temperature (5°C) have reasonably regular pores (Fig. 3(b-d)), diameters from 10 to 25 nm and an inter-pore distance of approximately 41 nm. The nano-sized pore structure is well developed and a uniform distribution of the nanopores can be observed.

As described by Nielsch *et al.*[46], the porosity or the pore fraction *P(f)* of the AAO structure can be estimated from equation (2).

$$P(f) = (2\pi/\sqrt{3}) \cdot (r/D_{\text{int}})^2 \tag{2}$$

where r and D_{int} are the pore radius and the inter-pore distance respectively. Since (r/D_{int}) is constant in a well defined AAO structure, the optimum porosity calculated from Fig. 2, where r = 9 nm and D_{int}=41 nm, is ~17.5%. However, slight changes in the concentration of acid in the electrolyte and temperature could shift the porosity due to the change in nature of acid attack on pore walls. Furthermore, the controlled adjustment of r and D_{int} by varying the applied potential has been observed. When increasing temperature or voltage, the pore diameter increased but this change was insignificant. However, as Nielsch *et al.* have shown, for alumina the inter-pore distance, D_{int}, is linearly proportional to the applied potential U (equation (3)) with a proportionality constant k of approximately k ~2.5 nm/V.

$$D_{\text{int}} = kU \tag{3}$$

With an applied potential of 17 V for the AAO sample in Fig. 2, D_{int} = 42.5 nm which correlates with the measured value of 41 nm. In contrast, the average pore diameter remained constant for different concentrations of sulphuric acid, suggesting the independent nature of the pore diameter

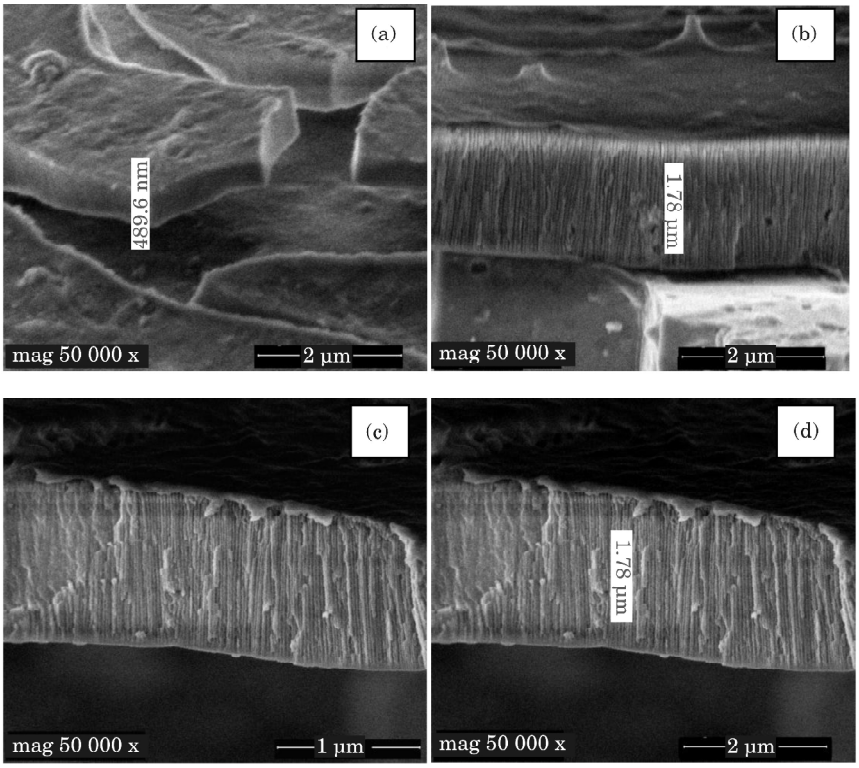

Fig. 5: Cross-section of AAO samples

from the acid concentration. As Masuda and Fukuda first reported, self-organized pore growth leads to a densely packed hexagonal pore structure for certain sets of parameters, as illustrated in Fig. 4(a).

Fig. 5 shows the cross-section images of AAO membranes fabricated in 0.3M H_2SO_4 acid under 23V at 10°C for 1h, 1.5 h and 3 h. In these images, an effective structure of the membrane can be seen. The pores are separately formed, perpendicular to the surface, and arranged in parallel columns, while the thickness of the AAO membranes increased with time.

3. NANOINDENTATION

Nanoindentation has been widely used for measuring mechanical properties such as the hardness and Young's modulus of test samples. This method makes use of very low loads in the milli-newton range. In a depth sensing indentation test, an indenter is pressed into the surface of a test solid and both the indenter load P and the indenter displacement h into the material are continuously recorded during the entire test. This provides a load-displacement curve *(P–h)*, which is a "fingerprint" of the mechanical

properties of the tested material, from which the hardness and elastic modulus can be calculated. A typical Micro Materials Nanotest would be equipped with a Berkovich (triangular pyramid) diamond tip with a nominal edge radius of ~100 nm. A schematic representation of a typical indentation *(P–h)* curve obtained with a Berkovich indenter is presented in Fig. 6(a). There are three important quantities that can be measured from the *(P–h)* curves: the maximum load, P_{max}, the maximum displacement, h_{max}, and the elastic unloading stiffness, $S = dP/dh$, defined as the slope of the upper portion of the unloading curve during the initial stages of unloading (also known as the contact stiffness). Another important quantity is the residual depth, h_r, which is the permanent depression after the indenter is fully unloaded.

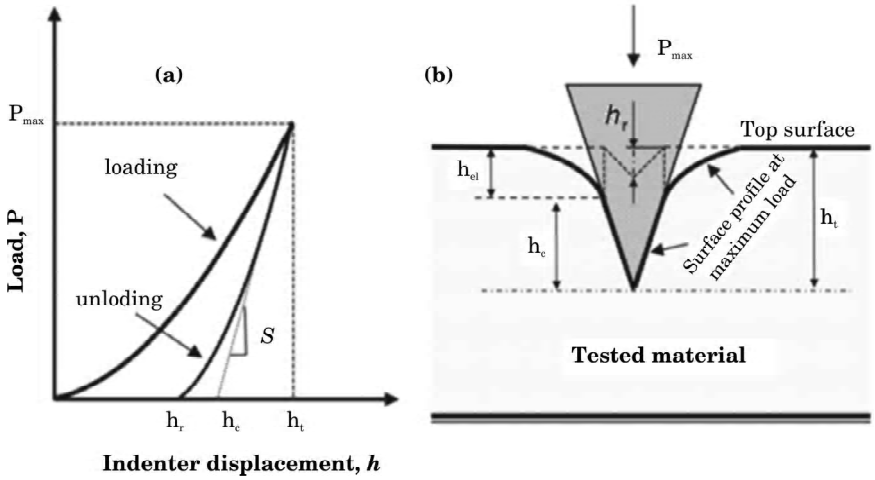

Fig. 6: A schematic illustration of indentation load-displacement curve with several important parameters used in the Oliver and Pharr analysis: (a) loading/ unloading cycle showing the main displacement parameters h_r, h_c and h_{max} (b) sectional view of the physical parameters under maximum load: h_{max} (maximum indenter displacement), h_c (indenter contact depth) and h_r (residual depth after complete unloading).

Fig. 6(b) shows the physical parameters of the indentation process in a cross sectional illustration in which it is assumed that the behaviour of the Berkovich indenter, can be modelled by a conical indenter with a half- angle, $\theta = 63.5°$. The corresponding *(P–h)* curves of three AAO specimens, anodised on H_2SO_4 acid electrolyte X, Y and Z at an indentation maximum displacement of 320 nm at room temperature, are shown in Fig. 7. The maximum displacement was limited to 320 nm in order to avoid distortion in the results from the non-oxidised Al metallic foils. The anodisation potentials for the three specimens were 20V and X and Z and 17V for Y whereas the concentrations of acid were 0.3M for X and Y while 1M for the specimen Z.

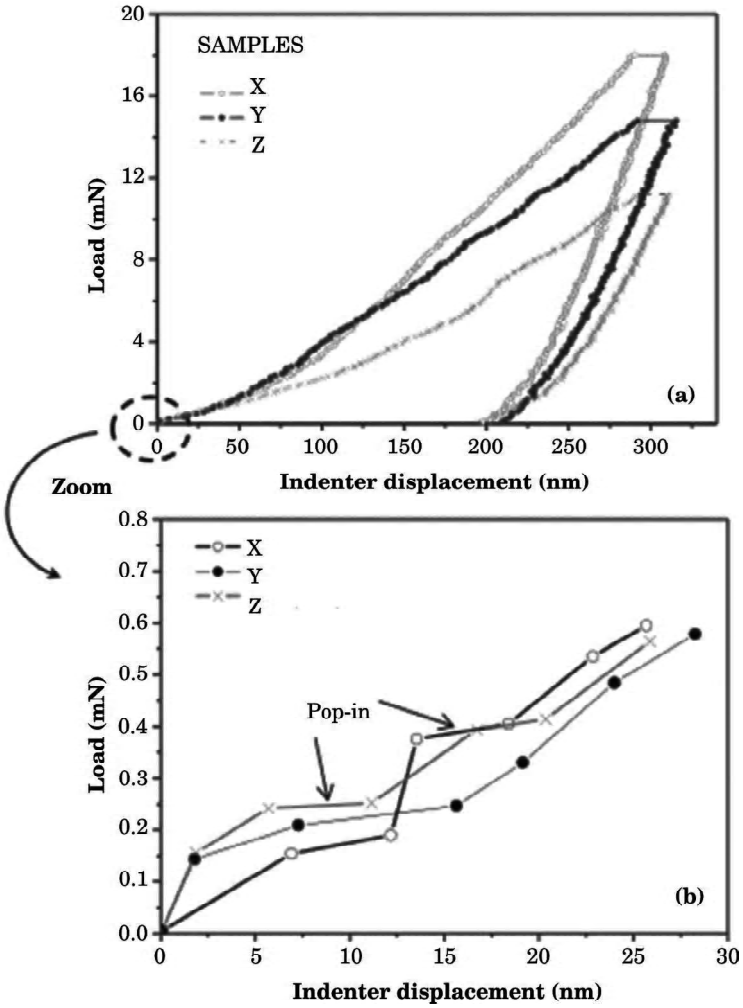

Fig. 7: Load–displacement curves of the nanoporous AAO samples X,Y and Z; (a) one complete cycle of loading and unloading and (b) expanded view of the first loading steps.

As the load increases, the indenter penetration displacement also increases (Fig. 7a). However, for a given applied load (during the loading stage), the indenter displacement is not the same for all the AAO specimens. In fact, for a given applied load, the indenter penetration is much smaller for the sample X in comparison with specimens Y and Z. This observation suggests that the specimen X is better able to withstand a state of deformation, the behaviour of which is ascribed to the differences of the AAO pore sizes achieved by using different deposition parameters. For a given applied load, the greater the pore diameter, the higher the material deformation is.

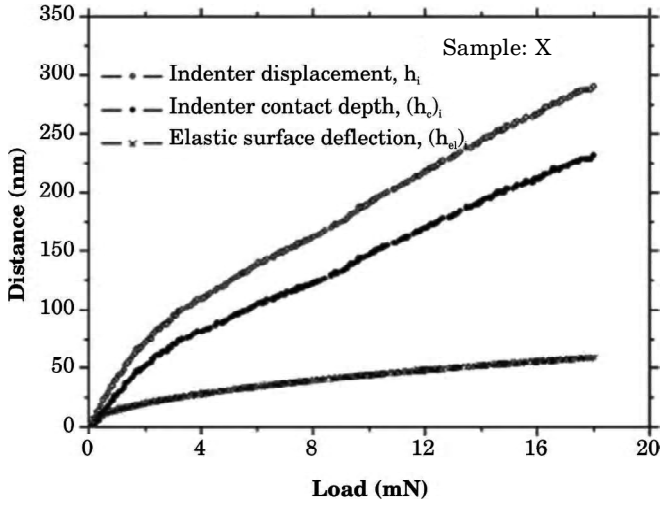

Fig. 8: The load versus displacement curve and graphical interpretation of the contact depth in specimen X.

In addition, as shown in Fig. 7b, the pop-in behaviour occurs at the beginning of the loading process. This behaviour, as Fang *et al*. described, (which is different from the dislocation-slip phenomenon) is due to the nanopore walls crashing one with another[47]. Although the indenter size is greater than the average pore or cell size, in the early stages of the applied load, the surface contact area between the indenter and the AAO material should be very small, which makes the average contact pressure higher than that of the rupture strength of the material, leading to the material collapse. Furthermore, the indentation results can be used to characterize the mechanical properties of the AAO samples by estimating the hardness and the Young's modulus of the specimens. The hardness H is the pressure exerted by the indenter at the maximum load $P_{\max}$ on the material, thus it is determined from the equation

$$H = \frac{P_{\max}}{A} \tag{4}$$

where A is the projected (or cross sectional) area of the indenter at a distance h_c back from its tip. The distance h_c is the depth along which contact is made between the indenter and the specimen. Under full load, the indenter is impressed to a total (maximum) depth $h_{\max}$, which can be taken from the load-displacement curve as indicated in the Fig. 6(a) and (b). After unloading is complete, there remains a residual depression of depth h_r, which is also given in the load-displacement curve.

Since the hardness defined to be based on the projected contact area under load, it may not be as same as the conventional hardness (measured

from the surface area of the residual hardness impression), if there is significant elastic recovery during unloading. The elastic modulus relates to contact area and the measured unloading stiffness[48] through the equation (5).

$$S = \beta \frac{2}{\sqrt{\pi}} E_r \sqrt{A} \tag{5}$$

where E_r, the 'reduced elastic modulus' (or the effective elastic modulus) can be given by:

$$\frac{1}{E_r} = \frac{1 - v^2}{E} + \frac{1 - v_i^2}{E_i} \tag{6}$$

The reduced elastic modulus takes into account the fact that elastic displacements occur in both the specimen and the indenter. The Young's modulus and the Poisson's ratio of the specimen and the indenter E, v *and* E_i, v_i respectively. The properties of the diamond indenter used are E_i = 1140 GPa and $\acute{\imath}_i$ = 0.07[49] and the Poisson's ratio of the AAO specimens is 0.22[22].

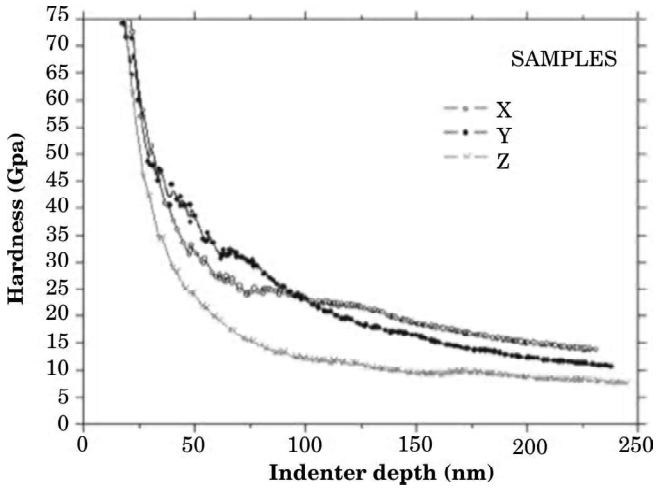

Fig. 9: Hardness as a function of the indenter depth.

The equation (5) is a general relation that applies to any axisymmetric indenter, where the dimensionless parameter, β, is used to account for deviations in stiffness caused by the lack of axial symmetry for pyramidal indenters[50,51]. Indentation experiments are often conducted with non-axisymmetric indenters, King used finite element simulations to estimate values for different indenter geometries[52]. He found that β = 1.034 for a triangular punch, the value which has been widely adopted for instrumented indentation testing with a Berkovich indenter.

Although the equations (5) and (6) have been used for isotropic materials and a partial effect from other directions exists in the transversely isotropic case, it is still possible to apply the equations to estimate the elastic constant in the indentation direction.The analysis used to determine the hardness, H, and elastic modulus, E, is an extension of the method proposed by Doerner and Nix that accounts for the fact that unloading curves are distinctly curved in a way that cannot be explained by the flat punch approximation[53]. Generally, in the flat punch approximation, the contact area remains constant as the indenter is removed, and the resulting unloading curve is linear. In contrast, experiments performed by Oliver and Pharr have shown that unloading curves are distinctly curved and usually well fitted by a specific power law[54]. The procedure used to measure H and E, following the work performed by Oliver and Pharr, is based on the unloading process shown schematically in Fig. 6(a), in which the elastic deflection, h_{el}, of the sample surface at the maximum load is given by:

$$h_{el} = \varepsilon \frac{P_{max}}{S} \tag{7}$$

where ε is a constant that depends on the geometry of the indenter and takes the numerical values of 1.00 for a flat punch, $\varepsilon = 0.72$ for a conical punch, and $\varepsilon = 0.75$ for a Berkovich indenter .

From the geometry of Fig. 6(b) that the depth along which, the contact is made between the indenter and the specimen, $h_c = h_{max} - h_{el}$, is:

$$h_c = h_{max} - h_{el} = h_{max} - \varepsilon \frac{P_{max}}{S} \tag{8}$$

In order to determine the hardness of a material, equation (4) should be used. However, since the definition of ardness is based on the projected contact area under load, Oliver and Pharr have defined an "area function", $F(h_c)$ that describes the projected (or cross sectional) area of the indenter at a distance, h_c, back from its tip. The area function is given by a multi-term polynomial fit of the form:

$$A = F(h_c) = \sum_{n=0}^{8} C_n \, (h_c)^{2-n} \tag{9}$$

For a perfect pyramid or cone the area function can be represented by the first term alone. By assigning the constant C_0 associated with the quadratic term to a value determined by the face angles of a Berkovich pyramid (with a half- angle of 65.3°), the resulting contact area is given by:

$$A = \left(3\sqrt{3} tan^2\theta\right) h_c^2 = 24.56 h_c^2 \tag{10}$$

Mean while, the monitoring of the average contact pressure is difficult due to the fact that the indenter displacement, rather than the contact depth, is measured during a nanoindentation test. The indenter displacement is the sum of the contact depth and the elastic deflection of the sample surface at the contact edge. It is therefore necessary to subtract the elastic deflection from each displacement measurement in order to calculate the average contact pressure. Oliver and Pharr technique, which is most often used to manipulate the nanoindentation test results, only provides the elastic deflection at the peak load. Thus, the procedure suggested by Novikov *et al.*[55] and Carneiro *et al.*[56] is used to monitor the average contact pressure during reloading of the indenter. The current actual value for the elastic deflection $h_{(el)i}$ of the sample surface at contact perimeter can be obtained as:

$$(h_{el})_i = h_{el}\,(P_i / P_{\max})^{1/2} \tag{11}$$

where P_i is the actual value of the applied load. The load dependence over the contact depth is found by subtracting the actual elastic deflection (calculated uing using equation (11)) from the actual displacement data, according to the following equation

$$(h_c)_i = h_i - h_{(el)i} \tag{12}$$

where $(h_c)_i$ is the actual contact depth and h_i the actual displacement at each indentation reloading point.

Mean while, the dependence of contact depth as well as the material surface elastic deflection over the applied load (under the loading process), is revealed in Fig. 8. The surface elastic deflection of the tested specimen increases slowly with the indenter displacement. However, for the same applied load, the magnitude of the contact depth is much more pronounced. In fact, at the peak load, the elastic deflection represents only 25% of contact depth. It can be noted that for an applied load smaller than 2.5 mN, the contact depth increases rapidly as a result of the crash of nanopore walls.

Hardness as a continuous function of penetration depth can be calculated in two steps. First, the elastic deflection of the sample surface at the peak load h_{el} has to be established using the Oliver and Pharr method. Then equation (12) can be substituted in equation (4) in order to calculate the actual hardness, H_i (see Fig. 8). The hardness values are obtained from all loading curve data points and correspond to the ratio between the actual applied loads and actual projected contact areas:

$$(H)_i = \frac{P_i}{24.56}[h_i - \varepsilon(P_{\max} / S)(P_i / P_{\max})^{1/2}]^{-2} \tag{13}$$

For the three specimens considered in this section, as demonstrated in Fig. 9, two regions can be highlighted on the hardness dependence over the indenter depth. In the first region, at a depth up to 75 nm, a significant decrease in hardness is observed. The hardness decreased from 75 GPa at a depth of ~ 20 nm to ~25 GPa for specimens X and Y and to ~ 15 GPa for specimen Z. However, from ~ 75 nm to 245 nm, the hardness decreases slowly with the indenter depth. Such behaviour in hardness suggests that these measurements should be made (ideally) using sharp indenters.

Since real pyramid indenters (such as Berkovich indenter) have a small rounded imperfection on its tip (inevitably occurs during its grinding process), for accurate measurements of hardness, the contact area between the indenter and the test material should be much larger when compared with the area of the defect at the indenter tip. This requirement is easy to attain for soft materials such as metals. However, for hard materials (oxides, carbides, nitrides etc.) at the beginning of an indentation experiment when the applied load is very low, the area of the defect at the indenter tip can eventually be comparable to contact area. Under this condition, it is expected that small tip-rounded indenters can have some influence on hardness calculations, since it can lead to the estimation of hardness with high magnitudes. For the tested AAO specimens, it was observed that the hardness increases substantially for loads lower than approximately 2 mN. Meanwhile, as the contact depth increases, the contact area between the indenter and the tested AAO material would surpasses the size of defects at the indenter tip reducing the hardness. This behaviour could also be a result of the fragile and porous structure of the AAO film, where the indenter penetrates the material; it is cracked to interior layers below the indenter tip. On the other hand, for the region between ~7 nm to 245 nm, the hardness remains almost constant despite the increase in indenter depth, therefore partly reflecting the mechanical properties of the crushed oxide. The porous structure of the AAO should lead to a deformation mechanism via crushed pores although the solid barrier layer may partially alleviate the crushed pores underneath the indenter. Moreover, for the region corresponding to the greater indenter penetration depths, the very steady hardness values suggest that the effect from the contribution of the substrate is not detected since the penetration depth is much lower than that of the film thickness. Fig. 9 also shows that the highest hardness value, calculated for maximum indenter penetration depth, was recorded for the sample prepared under the largest applied voltage.

The hardness, H, and Young's modulus, E of the AAO samples are given in Table 2. The hardness of the sample X is higher than that the sample Z and Y. This can be explained by the morphology of the surface of the samples, as previously mentioned.

The Young's moduli of the three nanoporous AAO samples, calculated for the highest indentation depth (of about 245 nm), are 131.2 GPa, 192.4

Table 2: Average hardness and Young's modulus calculated from indentation analysis.

Samples	*Hardness (GPa)*	*Young's modulus (GPa)*
Z	7.6	131.2
Y	10.6	163.2
X	13.7	192.4

GPa and 163.2 GPa, respectively. The Young's moduli obtained here are about 15% higher than those found elsewhere[57], primarily because the average pore diameter is smaller in this work than other studies. Additionally, the values of the Young's modulus herein obtained may also be associated with either absorbed moisture or residual water from the anodisation process, or the exposure to air.

4. CONCLUSIONS

Well-defined, self-ordered, porous alumina structures can be obtained by two-step electrochemical anodisation of Al electrodes in several electrolytes. Pores with smaller dimensions are obtained with sulphuric acid while phosphoric or oxalic acids produce pores with larger dimensions. Both anodisation time and applied potential affect the regularity and size of the nanopores, although the effect of the potential appears to be stronger than the effect of temperature in the transformation from crystalline alumina to amorphous alumina. While the inter-pore distance is linearly proportional to the applied potential, pore diameter remained independent of the acid concentration. Optimum pore growth was achieved with a pore fraction, $P(f)$~17.5%. This experimental pore fraction probably needs further optimising for improved pore ordering.

Where the mechanical properties of AAO structures are investigated using nanoindentation, the smallest pore diameter produces the highest hardness value. The analysis of the hardness–contact depth data reveals that the indentation hardness decreases in inverse proportion to the indenter penetration depth. Furthermore, the corresponding hardness remains constant despite the increase in indenter depth.

5. ACKNOWLEDGEMENTS

The authors would like to thank the FCT (Fundação para a Ciência e Tecnologia) for funding through the Ciencia 2007 programme and the pluriannual contract with CFUM and the European Commission through FP7-PEOPLE-2010-IRSES-NanoCIS (269279) project.

REFERENCES

[1] Thompson, D.W., Snyder, P.G., Castro, L., Yan, L., Kaipa, P. and Woollam, J.A. (2005). *J. App. Phys.,* 97: 113511–113519.

[2] Masuda, H. and Fukuda, K. (1995). *Science,* 268: 1466–1468.

[3] Son, H.Le., Angela, Camerlingo. and Hoa, T.M., Pham2, Behzad Rejaei1, Pasqualina M. Sarro, Anodic Aluminum Oxide Templates for Nanocapacitor Array Fabrication, slehoang@dimes.tudelft.nl.

[4] Kwang Hong, Lee., Yuan Peng, Huang. and Chee Cheong, Wong. (2011). *Electrochimica Acta*, 56: 2394–239.

[5] Hideki, Masuda. and Kazuyuki, Nishio. (2006). *Nanostructure Science and Technology*, pp. 296–312

[6] Belwalkar, A., Grasing, E., Van Geertruyden, W., Huang, Z. and Misiolek, W.Z. (2008). *Journal of Membrane Science*, 319: 192–198.

[7] Hideki, Masuda. and Kazuyuki, Nishio. (2006). *Nanostructure Science and Technology*, pp. 296–312.

[8] Youngdeuk, Kim., Bongbu, Jung., Hunkee, Lee., Hyejin, Kim., Kunhong, Lee. and Hyunchul, Park. (2009). *Sensors and Actuators B*, 141: 441–446.

[9] Thompson, D.W., Snyder, P.G., Castro, L., Yan, L., Kaipa, P. and Woollam, J.A. (2005). *J. App. Phys.,* 97: 113511–113519.

[10] Aricò, A.S., Bruce, P., Scrosati, B., Tarascon, J.M. and Schalkwijk, W.V. (2005). *Nature Mater,* 4: 366–377.

[11] Moon, J.M. and Wei, A. (2005). *J. Phys. Chem. B,* 109(49): 23336–23341.

[12] Dickson, R.M. and Lyon, L.A. (2000). *J. Phys. Chem. B,* 104: 6095–6098.

[13] O'Sullivan, J.P. and Wood, G.C. (1970). *Proc. R Soc. A,* 317: 511–543.

[14] Kirchner, A., MacKenzie, K.J.D., Brown, I.W.M., Kemmitt, T. and Bowden, M.E. (2007). *Journal of Membrane Science*, 287: 264–270.

[15] Feiyue, Li., Lan, Zhang. and Metzger Robert, M. (1998). *Chem. Mater,* 10: 2470–2480.

[16] Christof, Brandli., Jaramillo Thomas, F., Anna, Ivanovskaya. and McFarland Eric, W. (2001). *Electrochimica Acta*, 47: 553–557.

[17] Patermarakis, G. and Moussoutzanis, K. (2011). *J. Electroanal. Chem.,* 659: 176–190.

[18] Garcia-Vergara, S.J., Skeldon, P., Thompson, G.E. and Habazaki, H. (2006). *Electrochim. Acta,* 52: 681.

[19] Garcia-Vergara, S.J., Skeldon, P., Thompson, G.E. and Habazaki, H. (2007). *Surf. Coat. Technol*., 201: 9506.

[20] Cheng, Chuan. and Ngan, A.H.W. (2011). *Electrochimica Acta*, 56: 9998–10008.

[21] Sadasivan, V., Richter, C.P., Menon, L. and Williams, P.F. (2005). *AIChE Journal*, 51(2): 649–655.

[22] Fang, T.H. and Chang, W.J. (2003). *Microelectron Eng*., 65: 231–238.

[23] Xia, Z., Riester, L., Sheldon, W., Curtin, W.A., Liang, J., Yin, A. and Xu, J.M. (2004). *Rev. Adv. Mater Sci.,* 6: 131–139.

[24] Zhao, X., Seo, S.K., Lee, U.J. and Lee, K.H. (2007). *J. Electrochem. Soc.,* 154(10): C553–C557.

[25] Singh, G.K., Golovin, A.A. and Aranson, I.S. (2006). *Phys. Rev. B,* 73(20): 205422-1-205422-12

[26] Jessensky, O., Muller, F.d and Gosele, U. (1998). *Appl. Phys. Lett.,* 72(10): 1173–1175.

[27] Brown, F. and Mackintosh, W.D. (1973). *J. Electrochem. Soc.*, 120: 1096.

[28] Thompson, G.E., Xu, Y., Skeldon, P., Shimizu, K., Han, S.H. and Wood, G.C. (1987). *Phil. Mag. B*, 55: 651

[29] Su, Z.X., Hahner, G. and Zhou, W.Z. (2008). *J. Mater Chem.,* 18(47): 5787–5795.
[30] Chen, Z. and Zhang, H.G. (2005). *Journal of the Electrochemical Society*, 152: D227.
[31] Xin, Wang. and Gao-Rong, Han. (2003). *Microelectronic Engineering*, 66: 166–170.
[32] Belwalkar, A., Grasing, E., Van Geertruyden, W., Huang, Z. and Misiolek, W.Z. (2008). *Journal of Membrane Science*, 319: 192–198.
[33] Sousa, C.T., leitao, D., Ventura, J., Pereira, A.M., Amado, M., Sousa, J.B. and Araújo, J.P., Presented in 8ºENCMP Lamego (Portugal), Nanoporous Self-Organized Anodic Alumina Templates.
[34] Martín Jaime., Manzano Cristina, V. and Martín-González, Marisol. (2012). *Microporous and Mesoporous Materials*, 151: 311–316.
[35] Zaraska, Leszek., Sulka Grzegorz, D. and Jasku³a, Marian. (2010). *Surface and Coatings Technology*, 204: 1729–1737.
[36] Younghee, Na., Umme, Farva., Sung Min, Cho. and Chinho Park, Korean. (2009). *J. Chem. Eng.,* 26: 1785–1789.
[37] Sulka Grzegorz, D. (2008). *Nanostructured Materials*, 1–116 (WILEY-VCH Verlag GmbH & Co. KGaA, Weinheim).
[38] Fratila-Apachitei, L.E., Terryn, H., Skeldon, P., Thompson, G.E., Duszczyk, J. and Katgerman, L. (2004). *Electrochimica Acta*, 49: 1127–1140.
[39] Palibroda, E., Lupsan, A., Pruneanu, S. and Savos, M. (1995). *Thin Solid Films*, 256: 101–105.
[40] Bozhang, Yu. and Hulin, Li. (2002). *Materials Science and Engineering*, A325: 215–220.
[41] Lingchuan, Li. (2000). *Solar Energy Materials and Solar Cells,* 64: 279–289.
[42] Tsangaraki-Kaplanoglou, I., Theohari, S., Dimogerontakis, Th., Wang, Yar-Ming., Hong-Hsiang (Harry), Kuo. and Sheila, Kia. (2006). *Surface and Coatings Technology,* 200: 2634–2641.
[43] Fernandes, J.C.S., Picciochi, R., Da Cunha Belo, M., Moura e Silva, T., Ferreira, M.G.S. and Fonseca, I.T.E. (2004). *Electrochimica Acta*, 49: 4701–4707.
[44] Li, A.P., Muller, F., Birner, A., Nielsch, K. and Go, U. (1998). *J. Appl. Phys*., 84: 6023–6026.
[45] Leitao, D.C., Sousa, C.T., Ventura, J., Carpinteiro, F., Correia, J.G., Amado, M.M., Sousa, J.B. and Araujo, J.P. (2008). *Physics State Solid*, 5: 3488–3491.
[46] Nielsch, K., Choi, J., Schwirn, K., Wehrspohn, R.B. and Gosele, U. (2002). *Nano Lett*., 2: 677.
[47] Fang, T.H., Wang, T.H., Liu, C.H., Ji, L.W. and Kang, S.H. (2007). *Nanoscale Res. Lett.,* 2: 410–415.
[48] Oliver, W.C. and Pharr, G.M. (2004). *J. Mater Res.,* 19(1): 3–20.
[49] Simmons, G. and Wang, H. (1971). Single crystal elastic constant and calculated aggregate properties: A Handbook 2nd ed. The M.I.T. Press, Cambridge, Massachusetts
[50] Pharr, G.M., Oliver, W.C. and Brotzen, F.R. (1992). *J. Mater Res.,* 7: 613–617.
[51] Cheng, C.M. and Cheng, Y.T. (1997). *Appl. Phys. Lett.,* 71(8): 2623–2625.
[52] King, R.B. (1983). *Int. J. Solids Struct.,* 23: 1657–1664.
[53] Doerner, M.F. and Nix, W.D. (1986) *J. Mater Res.,* 1: 601–609.
[54] Oliver, W.C. and Pharr, G.M. (1992). *J. Mater Res.,* 7(6): 1564–1583
[55] Novikov, N.V., Dub, S.N., Milman, Y.V., Gridneva, I.V. and Chugunova, S.I. (1996). *Sverkhtverdye Materialy*, 18(3): 37–46. (English translation, *J Superhard Mater Allerton Press Inc*, New York 18(3): 32–40)
[56] Carneiro, J.O., Teixeira, V., Portinha, A., Dub, S.N. and Shmegera, R. (2004). *Rev. Adv. Mater Sci.,* 7: 83–90.
[57] Ko, S., Lee, D., Jee, S., Park, H., Lee, K. and Hwang, W. (2006). *Thin Solid Films*, 515: 1932–1937.